Annealing of SnO_2 thin films by ultra-short laser pulses

D. Scorticati,[1,*] A. Illiberi,[2] T. Bor,[1] S.W.H. Eijt,[3] H. Schut,[3] G.R.B.E. Römer,[1] D.F. de Lange,[4] A.J. Huis in 't Veld[1]

[1]*University of Twente, Faculty of Engineering Technology, 7500AE Enschede, The Netherland*
[2]*TNO Thin Film Technology, 5600HE Eindhoven, The Netherlands*
[3]*Delft University of Technology, Department of Radiation Science and Technology, 2629JB Delft, The Netherlands*
[4]*Universidad Autónoma de San Luis Potosí, Facultad de Ingeniería, C.P. 78290 San Luis Potosí, México*
[*]*d.scorticati@utwente.nl*

Abstract: Post-deposition annealing by ultra-short laser pulses can modify the optical properties of SnO_2 thin films by means of thermal processing. Industrial grade SnO_2 films exhibited improved optical properties after picosecond laser irradiation, at the expense of a slightly increased sheet resistance [Proc. SPIE 8826, 88260I (2013)]. The figure of merit $\phi = T^{10} / R_{sh}$ was increased up to 59% after laser processing. In this paper we study and discuss the causes of this improvement at the atomic scale, which explain the observed decrease of conductivity as well as the observed changes in the refractive index n and extinction coefficient k. It was concluded that the absorbed laser energy affected the optoelectronic properties preferentially in the top 100-200 nm region of the films by several mechanisms, including the modification of the stoichiometry, a slight desorption of dopant atoms (F), adsorption of hydrogen atoms from the atmosphere and the introduction of laser-induced defects, which affect the strain of the film.

OCIS codes: (140.3390) Laser materials processing; (140.7090) Ultrafast lasers; (310.6628) Subwavelength structures, nanostructures; (310.7005) Transparent conductive coatings; (350.6050) Solar energy.

References and links

1. D. Scorticati, G. R. B. E. Römer, T. Bor, W. Ogieglo, M. Klein Gunnewiek, A. Lenferink, C. Otto, J. Z. P. Skolski, F. Grob, D. F. de Lange, and A. J. Huis in 't Veld, "Optical and electrical properties of SnO_2 thin films after ultra-short pulsed laser annealing," Proc. SPIE 8826, Laser Material Processing for Solar Energy Devices **II**, 88260I (2013).
2. M. Batzill and U. Diebold, "The surface and materials science of tin oxide," Prog. Surf. Sci. **79**(2-4), 47–154 (2005).
3. R. Gordon, "Criteria for choosing transparent conductors," MRS Bull. **25**(08), 52–57 (2000).
4. S. F. Tseng, W. T. Hsiao, D. Chiang, K. C. Huang, and C. P. Chou, "Mechanical and optoelectric properties of post-annealed fluorine-doped tin oxide films by ultraviolet laser irradiation," Appl. Surf. Sci. **257**(16), 7204–7209 (2011).
5. W. Chung, M. O. Thompson, P. Wickboldt, D. Toet, and P. G. Carey, "Room temperature indium tin oxide by XeCl excimer laser annealing for flexible display," Thin Solid Films **460**(1-2), 291–294 (2004).
6. J. J. Kim, J. Y. Bak, J. H. Lee, H. S. Kim, N. W. Jang, Y. Yun, and W. J. Lee, "Characteristics of laser-annealed ZnO thin film transistors," Thin Solid Films **518**(11), 3022–3025 (2010).
7. G. Legeay, X. Castel, R. Benzerga, and J. Pinel, "Excimer laser beam/ITO interaction: from laser processing to surface reaction," Phys. Status Solidi **5**(10), 3248–3254 (2008).
8. C. W. Cheng, C. Y. Lin, W. C. Shen, Y. J. Lee, and J. S. Chen, "Patterning crystalline indium tin oxide by high repetition rate femtosecond laser-induced crystallization," Thin Solid Films **518**(23), 7138–7142 (2010).
9. M. F. Chen, K. M. Lin, and Y. S. Ho, "Effects of laser-induced recovery process on conductive property of SnO_2:F thin film," Mater. Sci. Eng. B **176**(2), 127–131 (2011).
10. B. D. Ahn, W. H. Jeong, H. S. Shin, D. L. Kim, H. J. Kim, J. K. Jeong, S. H. Choi, and M. K. Han, "Effect of excimer laser annealing on the performance of amorphous indium gallium zinc oxide thin-film transistors," Electrochem. Sol.- St. Lett. **12**, H430–H432 (2009).
11. J. Chae, L. Jang, and K. Jain, "High-resolution, resistless patterning of indium-tinoxide thin films using excimer laser projection annealing process," Mater. Lett. **64**(8), 948–950 (2010).
12. G. Haacke, "New figure of merit for transparent conductors," J. Appl. Phys. **47**(9), 4086–4089 (1976).

#204449 - $15.00 USD Received 8 Jan 2014; revised 27 Feb 2014; accepted 28 Feb 2014; published 12 Mar 2014

13. D. Scorticati, G. R. B. E. Römer, D. F. de Lange, and A. J. Huis in 't Veld, "Ultra-short-pulsed laser-machined nanogratings of laser-induced periodic surface structures on thin molybdenum layers," J. Nanophotonics **6**(1), 063528 (2012).
14. S. W. H. Eijt, R. Kind, S. Singh, H. Schut, W. J. Legerstee, R. W. A. Hendrikx, V. L. Svetchnikov, R. J. Westerwaal, and B. Dam, "Positron depth profiling of the structural and electronic structure transformations of hydrogenated Mg-based thin films," J. Appl. Phys. **105**(4), 043514 (2009).
15. A. Van Veen, H. Schut, J. de Vries, R. A. Hakvoort, and M. R. Ijpma, "Positron beams for solids and surfaces," AIP Conf. Proc. **218**, 171–196 (1990).
16. A. de Graaf, J. van Deelen, P. Poodt, T. van Mol, K. Spee, F. Grob, and A. Kuypers, "Development of atmospheric pressure CVD processes for high quality transparent conductive oxides," En. Proc. **2**(1), 41–48 (2010).
17. A. Borowiec and H. K. Haugen, "Subwavelength ripple formation on the surfaces of compound semiconductors irradiated with femtosecond laser pulses," Appl. Phys. Lett. **82**(25), 4462–4465 (2003).
18. J. Bonse, J. M. Wrobel, J. Kruger, and W. Kautek, "Ultrashort-pulse laser ablation of indium phosphide in air," Appl. Phys., A Mater. Sci. Process. **72**(1), 89–94 (2001).
19. Y. Jee, M. F. Becker, and R. M. Walser, "Laser-induced damage on single-crystal metal surfaces," J. Opt. Soc. Am. B **5**(3), 648–659 (1988).
20. V. Consonni, G. Rey, H. Roussel, and D. Bellet, "Thickness effects on the texture development of fluorine-doped SnO_2 thin films: The role of surface and strain energy," J. Appl. Phys. **111**(3), 033523 (2012).
21. B. Zhang, Y. Tian, J. X. Zhang, and W. Cai, "Structural, optical, electrical properties and FTIR studies of fluorine doped SnO_2 films deposited by spray pyrolysis," J. Mater. Sci. **46**(6), 1884–1889 (2011).
22. W. M. Hlaing Oo, S. Tabatabaei, M. D. McCluskey, J. B. Varley, A. Janotti, and C. G. Van de Walle, "Hydrogen donors in SnO_2 studied by infrared spectroscopy and first-principles calculations," Phys. Rev. B **82**(19), 193201 (2010).
23. J. R. Vig, "UV/ozone cleaning of surfaces," J. Vac. Sci. Technol. A **3**(3), 1027–1034 (1985).
24. R. Delhez, Th. H. de Keijser, and E. J. Mittemeijer, "Determination of crystallite size and lattice distortions through X-ray diffraction line profile analysis," Fresenius Z. Anal. Chem. **312**(1), 1–16 (1982).
25. B. E. Warren, *X-Ray Diffraction* (Addison Wesley, 1969).
26. M. Leoni, J. Martinez-Garcia, and P. Scardi, "Dislocation effects in powder diffraction," J. Appl. Cryst. **40**(4), 719–724 (2007).
27. C. V. Thompson, "Structure evolution during processing of polycrystalline films," Annu. Rev. Mater. Sci. **30**(1), 159–190 (2000).
28. R. Carel, C. V. Thompson, and H. J. Frost, "Computer simulation of strain energy effects vs. surface and interface energy effects on grain growth in thin films," Acta Mater. **44**(6), 2479–2494 (1996).
29. J. G. Berryman, "Bounds and self-consistent estimates for elastic constants of random polycrystals with hexagonal, trigonal, and tetragonal symmetries," J. Mech. Phys. Solids **53**(10), 2141–2173 (2005).
30. V. Consonni, G. Feuillet, and P. Gergaud, "The flow stress in polycrystalline films: Dimensional constraints and strengthening effects," Acta Mater. **56**(20), 6087–6096 (2008).
31. J. E. Dominguez, L. Fu, and X. Q. Pan, "Effects of crystal defects on the electrical properties in epitaxial tin dioxide thin films," Appl. Phys. Lett. **81**(27), 5168–5170 (2002).
32. W. Mao, B. Xiong, Y. Liu, and C. He, "Correlation between defects and conductivity of Sb-doped tin oxide thin films," Appl. Phys. Lett. **103**(3), 031915 (2013).
33. K. Liu, M. Sakurai, and M. Aono, "Controlling Semiconducting and Insulating States of SnO_2 Reversibly by Stress and Voltage," ACS Nano **6**(8), 7209–7215 (2012).
34. N. Laidani, R. Bartali, G. Gottardi, M. Andrele, and P. Cheyssac, "Optical absorption parameters of amorphous carbon films from Forouhi-Bloomer and Tauc-Lorentz models: a comparative study," J. Phys. Condens. Matter **20**(015216), 1–8 (2008).
35. A. I. Martinez and D. R. Acosta, "Effect of the fluorine content on the structural and electrical properties of SnO_2 and ZnO–SnO_2 thin films prepared by spray pyrolysis," Thin Solid Films **483**(1-2), 107–113 (2005).
36. C. Jacoboni, *Theory of Electron Transport in Semiconductors*, Springer Series in Solid-State Science, Vol. **165** (Springer, 2010).
37. V. I. Kaydanov, T. J. Coutts, and D. L. Young, Studies of Band Structure and Free-Carrier Scattering in Transparent Conducting Oxides Based on Combined Measurements of Electron Transport Phenomena," NREL/CP-520–29064 (2000).
38. A. Oprea, E. Moretton, N. Barsan, W. J. Becker, J. Wollenstein, and U. Weimar, "Conduction model of SnO_2 thin films based on conductance and Hall effect measurements," J. Appl. Phys. **100**, 033716 (2006).
39. H. M. Ng, D. Doppalapudi, T. D. Moustakas, N. G. Weimann, and L. F. Eastman, "The role of dislocation scattering in n-type GaN films," Appl. Phys. Lett. **73**(6), 821–823 (1998).

1. Introduction

Tin-dioxide (i.e. SnO_2), also known as stannic oxide, is a widely applied and studied ceramic material [2]. Un-doped and stoichiometric SnO_2 is a semiconductor with a wide bandgap (~3.6 eV). Shallow doping of SnO_2 (e.g. with F, Cl or Sb) or small shifts from its perfect stoichiometry (i.e. SnO_{2-x}, with $x < 1$), which are associated with oxygen vacancies, lead to *n*-type semi-conductive behavior. Doped SnO_2 combines a high electrical conductivity with

#204449 - $15.00 USD Received 8 Jan 2014; revised 27 Feb 2014; accepted 28 Feb 2014; published 12 Mar 2014

optical transparency and belongs to a class of materials referred to as Transparent Conductive Oxides (TCOs). These TCOs are important for opto-electronic devices [2, 3]. Due to the low fabrication cost, SnO_2 thin films find application in different areas, including glass coatings for thermal insulation, oxidation catalysts, gas sensors, flat panel displays, touch panels, flexible electronics, dye-sensitized solar cells (DSSC), thin film silicon and cadmium telluride (CdTe) solar cells, light-emitting diodes (LEDs), etc [3]. A strong interest for TCO materials led research into the effects of post deposition annealing by nanosecond (ns) laser pulses on the optical and electrical properties of different TCOs [4–11]. The use of Rapid Thermal Laser Annealing (RTLA) is an alternative process to conventional furnace annealing. Compared to furnace annealing RTLA reduces thermal damage of sensitive low cost substrates with low melting points [4]. For a given wavelength of the laser radiation, ultra-short laser pulses -with pulse durations in the order of tens of picoseconds or less- can induce same high surface temperatures of the film, but at a significantly lower energy input per pulse, when compared to nanosecond laser pulses. This can be attributed to the fact that the Heat Affected Zone (HAZ) due to ultra-short laser pulses is significantly smaller than due to ns laser pulses. Hence, ultra-short laser pulsed processing is highly selective in depth of the laser induced transformations. This can be exploited for processing either thin films or selectively process a thin top layer of the substrate under consideration. Moreover, due to the small timescales at which the annealing process occurs during ultra-short laser processing, new and original material structures can be obtained. Despite low heat input during laser annealing, heat accumulation might occur, especially at high pulse rates. However, by careful selection of the laser parameters (i.e. laser fluence, repetition rate, and pulse overlap), heat accumulation can be controlled in order to increase the duration of the heating cycle time, while ensuring that the temperature at the film/substrate interface remains below the damage threshold for the substrate.

Laser annealing is an alternative use of ultra-short pulsed laser sources, as a future prospect, in thermal processing, e.g.: extremely selective annealing, laser selective evaporation (either for removal of unwanted impurities or for tailoring the stoichiometry), ‘ultra-selective’ laser doping, etc. To fully exploit this alternative use of ultra-short pulsed laser sources, a detailed understanding is required of the heat-related phenomena in a laser fluence range below the ablation threshold and their effects on the material.

In an earlier study [1], the effects of UV (λ = 343 nm) picosecond (ps) laser irradiation on the macroscopic optical and electrical properties of thin SnO_2 films was demonstrated and discussed. It was shown that the total average optical transmittance (T) in the wavelength range from 400 to 1100 nm increased from 71.4% to 76.1%, while the electrical properties were only slightly deteriorated. That is, the sheet resistance (R_{sh}) increased from 13.5 to 16.1 Ω/sq. The Figure-of-Merit $\phi = T^{10} / R_{sh}$ [12], which combines the optical and electrical properties in a single performance quantity, increased up to 59% due to the laser treatment. Moreover, it was found that when nanostructures (also known as Laser-Induced Periodic Surface Structures, or LIPSS) form on the surface of the film, due to the laser irradiation, the optical reflectivity of the film reduces and the haze of the film increases. This was attributed, in part, due to the morphology of LIPSS, which was superimposed on the original morphology. Other possible causes, which could smoothen the mismatch of refractive index with air, as well as could explain the decreased optical absorption by the bulk of the material, were not discussed [1]. Moreover, it was also pointed out that processing with ultra-short pulses may introduce microscopic modifications in the lattice, which do result in measurable changes in optical and electrical properties.

The present research aims to study the effect of UV (λ = 343 nm) picosecond laser-material interaction on the microscopic structure of SnO_2 thin films in order to explain the origin of the macroscopic changes observed in the optical, as well as electrical properties of the film. We discuss the causes at the atomic scale, which can explain the observed decrease of conductivity, such as modification of the density of oxygen vacancies, changes in average grain size, amorphization due to fast quenching, introduction of quenched-in defects during fast thermal processing, as well as stress/strain induced by the defects in the lattice. Also the

#204449 - $15.00 USD Received 8 Jan 2014; revised 27 Feb 2014; accepted 28 Feb 2014; published 12 Mar 2014

observed changes in the refractive index n and extinction coefficient k can be understood at the atomic level. That is, the presence of detrimental impurities, formation of different material phases, presence of amorphous structure of the lattice and different carrier densities. The possible causes, which induce a modification of the carrier density, electronic mobility and optical constants n and k, due to the laser treatment, were examined by means of several inspection techniques. The results of these analyses were cross-checked to give an overall exhaustive comprehensive interpretation of the observed effects. The results of this study can be used to further improve the performance of SnO_2-based electrodes for solar cells and/or other electronic devices.

2. Experimental

2.1 Laser setup

In the experiments, an Yb:YAG laser source was used, showing a nearly Gaussian power density profile ($M^2 < 1.3$) and with fixed pulse duration of about 6.7 ps. A Third Harmonic Generation (THG) unit was employed to convert the central wavelength $\lambda = 1030$ nm of the laser source to 343 nm (UV) and a Galvano-scanner, equipped with an F-theta-lens (focal length 103 mm), was used to scan the focal spot (diameter $d = 17$ μm) over the surface of the samples. The spot diameter, combined with the scan velocity v and the pulse frequency f_p determine the spatial pulse-to-pulse overlap (OL), which is defined here as $OL = 1 - v / (d \cdot f_p)$. More details on the experimental laser setup can be found in [13].

2.2 Analysis tools

Several analysis techniques were adopted to study the effects of the laser radiation on the material. A high resolution Scanning Electron Microscope (SEM), as well as an Atomic Force Microscope (AFM) were utilized to investigate the surface morphology of the samples, as well as their cross sections. For the investigation of the crystalline structure of the outermost atomic layers, Transmission Electron Microscope (TEM) was used. X-ray diffraction (XRD) experiments were performed on a system using a mixture of $K\alpha_1$ and $K\alpha_2$ of Co radiation with an average wavelength of $K\alpha = 0.17903$ nm, to determine the crystallographic structure of the film. To identify changes in stoichiometric composition of the SnO_2 thin films and the concentration of impurities, we employed X-ray photoelectron spectroscopy (XPS). Depth profiling of impurities with low concentrations was performed using the Time of Flight Secondary-Ion Mass Spectrometry (TOF-SIMS) technique. The electrical properties of the films, such as electron mobility, carrier density and sheet resistance, were determined by Hall effect measurements and the 4-point probe technique. Last, positron annihilation was adopted to inspect the occurrence of laser-induced defects in the layers after the laser treatment. The Doppler broadening of positron annihilation radiation was measured with a low-energy Variable Energy Positron beam (VEP) using positrons with a kinetic energy in the range of 0-25 keV [14]. The depth profiles of the S and W parameters, extracted from the Doppler broadened 511 keV γ-ray photopeak, were analyzed using VEPFIT software [15].

2.3 Samples

Fluorine-doped SnO_2 samples of 980 nm thickness, deposited by chemical vapor deposition (CVD) on 1 mm thick Borofloat®-glass, showing a sheet resistance of $R_{sh} = 13.5$ Ω/sq were used. This combination of a thin SnO_2 layer on glass is used for the production of silicon thin film solar cells. Deposition of the samples was performed at TNO in the Netherlands using an industrial process [16].

2.4 Experimental approach

The experimental procedure consisted of three steps. During the first step, laser tracks were created with varying pulse-to-pulse overlap (OL), number of over-scans (OS) and fluence levels (being F_0 the peak fluence) by scanning the focal spot over the sample at a fixed pulse repetition frequency of $f_p = 100$ kHz. The second step consisted of finding conditions for

#204449 - $15.00 USD Received 8 Jan 2014; revised 27 Feb 2014; accepted 28 Feb 2014; published 12 Mar 2014

damage-free (crack-free and no ablation) treatment of the films. This second step was iterated by choosing finer variation of the processing parameters (OL, OS and fluence) and inspecting the sample afterwards by SEM. The third and final step of the experimental procedure consisted of creating laser treated (3 cm^2) areas by varying the pitch (distance) between parallel laser tracks. Following this procedure, three sets of samples were manufactured and subjected to subsequent analysis:

1. As-deposited SnO_2, without laser treatment applied;
2. Low fluence regime (F_0 = 0.17 J/cm^2, 1 OS, OL = 98.7%, pitch = 3 μm);
3. High fluence regime (F_0 = 0.26 J/cm^2, 1 OS, OL = 98.7%, pitch = 3 μm).

3. Results and discussion

3.1 Surface morphology

When comparing the results of SEM and AFM measurements of the as-deposited SnO_2 sample (Fig. 1(a) and Figs. 2(a)-2(b)) to the results of the low fluence samples (Fig. 1(b) and Figs. 2(c)-(d)), only small differences are observed. However, a clearly modified surface morphology is found for the sample treated at high laser fluence (Fig. 1(c) and Figs. 2(e)-2(f)). As already discussed in our previous work [1], the nano-structures observed in Fig. 1(c) and Figs. 2(e)-2(f) on the SnO_2 film treated at high laser fluence are Laser-induced Periodic Surface Structures (LIPSSs). In particular, the obtained LIPSSs were identified as High Spatial Frequency LIPSSs (HSFLs) [17].

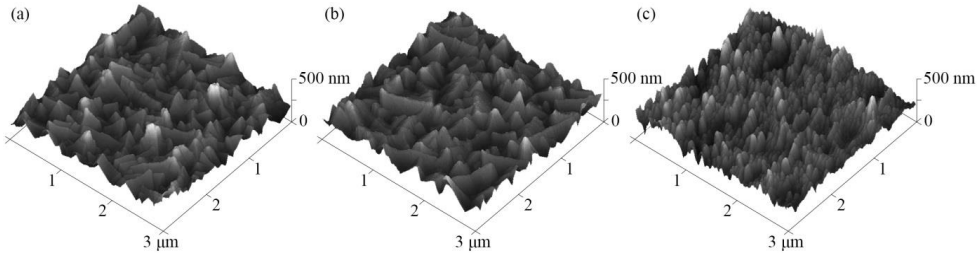

Fig. 1. AFM measurements of the three samples. (a) as-deposited SnO_2, (b) SnO_2 treated at low laser fluence and (c) at high laser fluence.

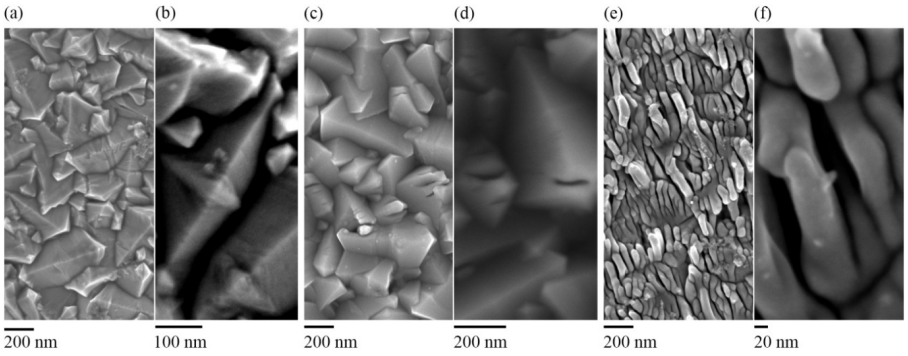

Fig. 2. SEM images of the three samples. (a) and (b) show as-deposited SnO_2 surface at different magnifications. (c) and (d) show SnO_2 treated at low laser fluence sample at different magnifications. (e) and (f) show SnO_2 treated at high laser fluence sample at different magnifications.

For the sample treated at low fluence, where no LIPSSs were found (see Fig. 2(c)), the material remained entirely in the solid state during annealing. In the case of treatment at high fluence, LIPPSs were formed, which only happens when either melting and/or ablation occurs

#204449 - $15.00 USD Received 8 Jan 2014; revised 27 Feb 2014; accepted 28 Feb 2014; published 12 Mar 2014

due to laser irradiation. In both cases, the melting temperature must be reached to observe morphological modifications. Therefore, the maximum surface temperature reached during the laser processing of the sample treated at high fluence is expected to have exceeded the melting temperature T_M. Several mechanisms can induce melting of the surface in the sample treated at high fluence. First, if the peak fluence F_0 of a single pulse is above the fluence F_M, required for melting, the surface melts after one single pulse. Experiments based on the so-called D^2-method [18] were performed to identify the single pulse melting fluence threshold to equal $F_M = 0.56$ J/cm^2. As the single peak fluence F_0 applied during the experiments (see section 2.4) was well below F_M, other mechanisms should be considered to explain the occurrence of surface melting. Two other mechanisms are most likely inducing the melting of the surface. First, inter-pulse heat accumulation and secondly, a reduction of the melting threshold due to laser induced defects when a high overlap (OL) is applied. Usually, a reduction of the thresholds of melting and ablation is observed only upon irradiation with hundreds to thousands of laser pulses. This particular phenomenon is explained by the formation of numerous defects just below the surface of the irradiated material, which in turn reduces the thresholds [19]. The latter can also be understood as the chemical storage of heat in the material, by increasing the free Gibbs energy of the lattice, induced by an increasing disorder. However this reduction of the threshold for melting is expected to be a small fraction of F_M. At $F_0 = 0.26$ J/cm^2, corresponding to the high laser fluence condition, the ratio between the peak fluence and the fluence for melting is small, i.e. $F_0/F_M \approx 0.5$. For ultra-short laser pulses, thermal dissipation due to heat conduction in the material is limited during the pulse. Hence, the maximum surface lattice temperature T_0 of SnO_2 at the center of the focal spot ($r = 0$, $z = 0$) at $F_0 = 0.26$ J/cm^2 will be $T_0 \approx T_M/2$. The significant difference between T_M and T_0 cannot be explained by a reduction of the melting temperature in SnO_2 caused by the accumulation of defects with the current laser conditions. Therefore, the difference implies that heat accumulation occurs during the treatment and explains why the top surface of the film is melted. That is, heat accumulation allows to reach temperatures above the single-shot maximum temperature, which can explain observed surface modifications of the material after being irradiated with pulses having fluence levels $F_0 < F_M$. Moreover, the final structure of a material after the annealing process depends on the local thermal history of the heating-quenching cycle. The occurrence of controlled inter-pulse heat accumulation, which rules the timescale of the annealing cycle, is an important condition to prevent amorphization in material processing via ultra-short laser pulses. On the other hand, it should be mentioned that heat accumulation needs to be controlled by varying the laser parameters (e.g. λ, f_p and F_0) in order to avoid damage of thermally sensitive substrates.

3.2 Cross sections

SEM pictures of the cross sections (Fig. 3) show that the grain morphology in the bulk (close to the glass) of the sample treated at high fluence is similar to the morphology of the as-deposited sample. In both samples, small grains are visible near the glass substrate due to the fast nucleation process during deposition. Grain growth along a preferential direction with lower formation energy enables the development of bigger V-shaped grains on top of the small ones. XRD texture measurements performed on the samples indicated the presence of a strong fiber texture with <301> in the direction normal to the plain of the sample. This type of texture has been observed before [20] and is enhanced in relatively thick (over 500 nm) SnO_2:F layers. The fiber texture was not significantly changed due to the laser irradiation. However, the top 100-200 nm of the high fluence laser-treated sample reveals a different contrast and structure than the as-deposited sample.

Arguably, the difference in contrast of the top 100-200 nm in Fig. 3(b) can be attributed either to an increased amount of defects, or to a different chemical composition in the top layer, as a result of a modified lattice structure in the high fluence sample. To investigate the possible presence of an amorphous lattice structure within the modified top part of the high fluence sample, due to fast quenching, the as-deposited and the high fluence samples were glued together and a lamella for TEM inspection was extracted and subsequently

#204449 - $15.00 USD Received 8 Jan 2014; revised 27 Feb 2014; accepted 28 Feb 2014; published 12 Mar 2014

mechanically grinded and ion milled. The cross sections of the two samples are shown in Figs. 4(a) and 4(d). Figures 4(b) and 4(e) show a close-up view of the surface layers at the SnO_2-glue interface, where lattice fringes indicate crystallinity of the samples all the way up to the surface. The latter is supported by the corresponding electron diffraction pattern recorded near the interfaces shown in Figs. 4(c) and 4(f), showing no amorphous halo. This result was also confirmed by XRD spectra, where no amorphous hump was observed when the same sample was inspected not locally, but over a bigger area (1 × 1 cm) [1]. Hence, both measurements indicate the absence of any amorphous structure in the lattice. Therefore, any observed effect of the laser process on the optical and electrical properties of the film cannot be attributed to amorphization.

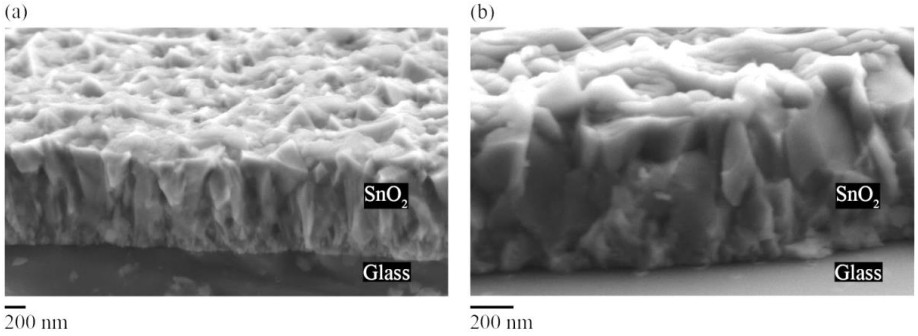

Fig. 3. Cross section of SEM images of (a) as-deposited SnO_2, (b) SnO_2 treated at high laser fluence causing surface melting and the LIPSSs depicted in Figs. 2(e) and (f).

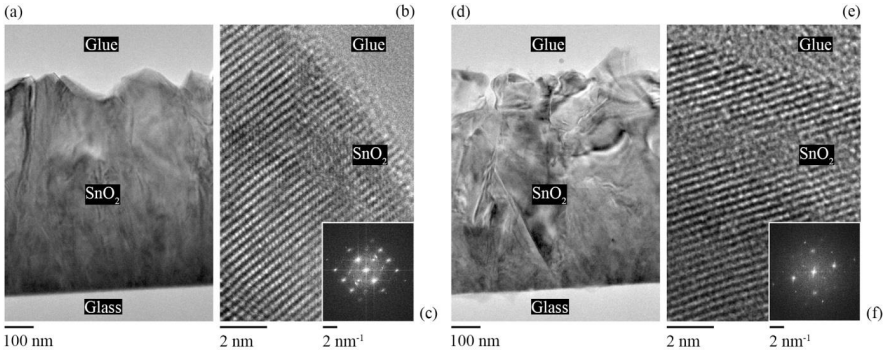

Fig. 4. (a) and (b): Bright field TEM images of as-deposited SnO_2 at two different magnifications. (d) and (e): Bright field TEM images of the sample treated with high laser fluence at two different magnifications. Pictures (c) and (f) show the electron diffraction pattern recorded near the interfaces, respectively corresponding to the as-deposited and high fluence samples.

3.3 Stoichiometry and chemical composition

The optical and electrical properties of an SnO_2 film greatly depend on its stoichiometry and chemical composition. Small shifts of stoichiometry, as well as the presence of impurities are associated to interstitial states and band tailing effects. Those can affect the transmittance of light in the bandgap of a semiconductor, as well as the carrier density and the electron mobility of the material. The latter are significant quantities contributing to the sheet resistance (R_{sh}), being $R_{sh} = 1 / (n_e \mu_e q_e t)$, where n_e, μ_e, q_e and t respectively are the carrier density, the electron mobility, the electron charge and the thickness of the film. Therefore, to study the effect of laser annealing on the chemical composition and stoichiometry, we carried out XPS and TOF-SIMS analysis of the samples.

#204449 - $15.00 USD Received 8 Jan 2014; revised 27 Feb 2014; accepted 28 Feb 2014; published 12 Mar 2014

Oxygen desorption was inspected by the XPS technique. Tin and oxygen concentrations were measured along the depth of the samples and their signals (respectively the Sn1d5 and O1s peaks) were divided in order to have their ratio O/Sn, see Fig. 5. In perfectly stoichiometric SnO_2, this ratio is 2. Irrespective of the fluctuations of the signals over depth, we observed a relative decrease of oxygen concentration in the laser-treated sample at high fluence compared to the concentration on the as-deposited film. The largest shifts in the stoichiometry from SnO_2 to SnO_{2-x}, with x as high as 0.1, were found in the sample treated with high fluence, but only in the top 250 nm of the film. We attribute this effect to desorption of surplus interstitial oxygen from the film during laser processing.

Traces of dopants and/or impurities in the SnO_2 matrix were measured by TOF-SIMS analysis, see Fig. 6. TOF-SIMS measurements were performed over 50 × 50 μm spots, over the full depth of the layers. Fluorine (F) and hydrogen (H), known to act as n-doping impurities [21, 22], were found to be present in the samples. As impurities of F were not detected by XPS, it can be concluded that their concentrations are below the sensitivity (0.1% at) of the instrument. Measured concentrations of F dopant atoms as function of depth were not showing appreciable changes in the shape of their concentration profiles between the three samples, with a typical peak at the SnO_2/glass interface. Concentration profiles of H atoms over the depth of the sample treated at high-fluence display an appreciably increased density at the surface, compared to the as-deposited sample indicating an adsorption of H from air during the laser treatment. Diffusivity of impurities in a host material is related to the type of impurity and the state (liquid or solid) of the host material. Several orders of magnitude distinguish the diffusivity in the solid state from the diffusivity in the liquid state. Interestingly, the concentration over depth of the adsorbed H in the high fluence sample is not step-like. This implies that the time of resolidification of the laser-material interaction zone is faster than the time required by the dopant to reach the opposite end of the molten region. The latter implies that the molten state is reached for brief periods just after the laser pulse. Due to its atomic small size, H has the highest diffusion coefficient among the other atomic species present in atmosphere. Therefore its adsorption into the SnO_2 matrix will be the largest among the atmospheric species. Since the number of experimental counts in TOF-SIMS analysis is linearly proportional to the relative amount of impurities in the material, we integrated the counts in Fig. 6 along the depth and subsequently divided these values with respect to the thickness, in order to obtain an average density of each impurity. Calculated data were normalized by the averaged values found for the as-deposited sample. Table 1 lists the relative quantities of F and H in the three samples. As can be observed, the relative amounts of F and H show different trends with the applied laser fluence. On the one hand, the total amount of F reduces slightly in both laser-treated samples, with increasing laser fluence due to desorption. On the other hand, the total amount of H increases due to adsorption from the atmosphere, following the increase of the laser fluence applied.

Table 1. From left to right: (i) Measured electrical properties of the as deposited (AD), low fluence (LF) and high fluence (HF) samples, (ii) Integrated counts of F, H and C from SIMS measurements of signals relative to different impurities found in the three samples, (iii) optical average transmittance T and reflectance R in the wavelength range from 400 to 1100 nm from previous investigation [1] and (iv) figure of merit ϕ [1]. Carrier density n_e and electron mobility μ_e were measured by Hall technique (considering less than 5% instrumental error on the values), while sheet resistance R_{sh} was measured also by 4 point probe technique [1]. Percentile quantities in parenthesis in the carrier density, electron mobility and figure of merit columns show the relative shifts from the as-deposited layer.

	$n_e \times 10^{20}$ [cm^{-3}]	μ_e [$cm^2V^{-1}s^{-1}$]	R_{sh} [Ω/sq]	F	H	C	T [%]	R [%]	$\phi \times 10^3$ [Ω^{-1}]
AD	2.32	19.1	13.5 ± 0.5	1	1	1	71.4	9.9	2.55
LF	2.07(-8.6%)	20.0(+4.7%)	14.6 ± 0.5	0.97	1.17	0.65	73.3	8.6	3.05(+20%)
HF	2.17(-4.3%)	17.2(-9.9%)	16.1 ± 0.5	0.95	1.48	0.39	76.2	7.2	4.07(+59%)

#204449 - $15.00 USD Received 8 Jan 2014; revised 27 Feb 2014; accepted 28 Feb 2014; published 12 Mar 2014

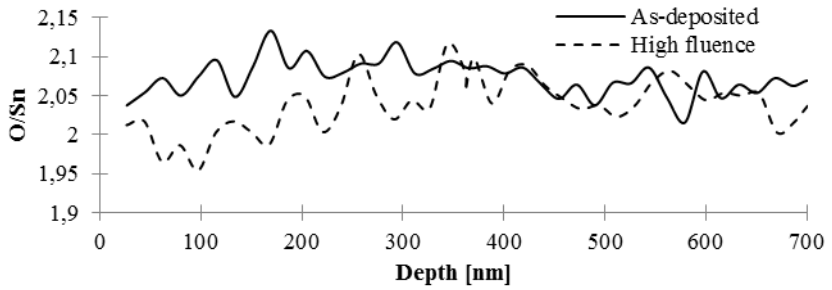

Fig. 5. O/Sn ratio from XPS measurements for the as-deposited SnO_2 and the sample treated at high fluence.

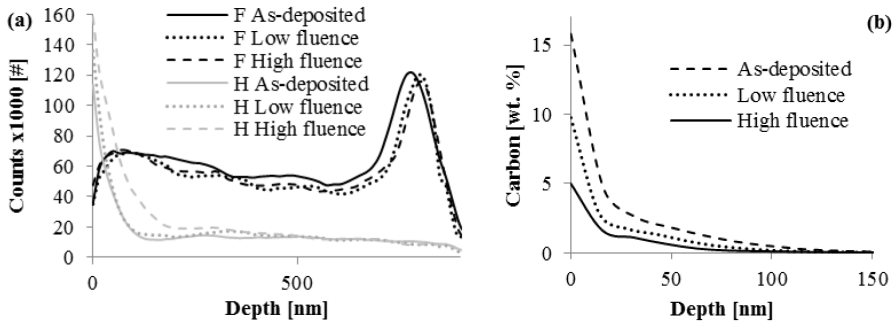

Fig. 6. TOF-SIMS results showing the concentrations of different impurities as a function of depth.

Combined results from the XPS and TOF-SIMS analysis indicated the presence of carbon in the three samples, see Fig. 6(b). A high concentration of carbon was found at the surface of the as-deposited sample, quickly decreasing within the first 150 nm into the film. The latter distance matches with the measured transition from air to bulk SnO_2 from measured AFM data, as shown by the cumulative height distributions in our previous work [1]. This observation limits unambiguous interpretation of the actual carbon distribution in the samples. Two different interpretations of Fig. 6(b) are given. First, carbon is simply intermixed in SnO_2 up to the depth measurable by TOF-SIMS. Secondly, carbon is present as a very thin superficial coating (few tens of nanometers) after deposition, intermixed with SnO_2 just in the outermost atomic layers. In the latter case, the carbon signal is measured also at deeper depths since the superficial roughness affects the uniformity of the sputtering. The latter explanation would also fit with the concentration of carbon over depth. That is, Fig. 6(b) shows two different concentration slopes, which intersect at a depth of about 25 nm. Comparing the three samples, a significantly higher concentration of carbon within the first 150 nm was found in the as-deposited material than in the laser treated samples. The concentration reduces with increasing laser fluence (see Table 1 and Fig. 6), similarly to elsewhere reported [23]. Since the TOF-SIMS analysis shows only counts, XPS was adopted to obtain an absolute value of the carbon concentration. At the surface, the XPS signals showed a reduction of carbon concentration from 44% at. (15.8% wt.) in the as-deposited SnO_2 to 19.8% at. (4.99% wt.) in the SnO_2 treated at high fluence. It was found that, after the first 150 nm, TOF-SIMS counts showed a rather constant and similar profile in all samples (see Fig. 6). The high concentration of carbon in the as-deposited sample cannot be simply attributed to atmospheric contamination, but must have been caused by the carbon-rich precursor gases used during the CVD process in the last deposition stage of the SnO_2 layers [16]. Moreover, the crystalline structure of the outermost layers would not explain atmospheric contamination.

#204449 - $15.00 USD Received 8 Jan 2014; revised 27 Feb 2014; accepted 28 Feb 2014; published 12 Mar 2014

3.4 Lattice structure and presence of strain

X-ray Diffraction (XRD) was employed to obtain an average value of the SnO_2 grain size for the different samples. The grain size can be determined from the width of the measured XRD reflections since the grain size is inversely proportional to the width (the so-called "coherent length"), if no other sources of broadening are present. Often, significant contributions to the total broadening arise from the non-ideal optics of the diffractometer and the wavelength distribution ("instrumental broadening") and/or from microstructural sources such as dislocations introducing non-homogeneous strain fields ("strain broadening"). The contribution from the instrument can be removed using separately measured reflections of a standard material employing the same instrumental configuration and X-ray wavelength. Here, a standard sample, LaB_6, was used for this purpose and an interpolation routine was employed to determine the instrumental line profile for the measured reflections. Subsequently, a deconvolution procedure was adopted to obtain the Fourier coefficients of the only structural broadened profiles [24]. The widths of these profiles were characterized by the integral breadths determined from the Fourier coefficients. A plot of the integral breadths as a function of $1/d_{\{hkl\}}$, with $d_{\{hkl\}}$ being the lattice spacing pertaining to the $\{hkl\}$ reflection considered, is shown in Fig. 7 for all the samples. If grain size broadening is the only source of structural broadening, then it can be shown [25] that the integral breadths of all SnO_2 reflections are equal. However, Fig. 7 shows that the integral breadth increases as a function of $1/d_{\{hkl\}}$ for all samples. Consequently, the samples exhibit lattice defects causing "strain broadening". For the purpose of this study, we adopted a relatively straightforward approach to separate the "size" and "strain" sources employing multiple orders of the same reflection. Hence, the integral breadth values of the {110} and {220} SnO_2 reflections are extrapolated towards the intercept at $1/d_{\{hkl\}} = 0$ [20]. The so-obtained values represent the net broadening due to the small size of SnO_2 crystallites oriented with their <110> normal to the plane of the sample. Here, the integral breadths of the samples are approximately equal to 0.015 nm^{-1} resulting in an average grain size of 67 nm, when adopting a Scherrer constant equal to one. These results match with the observed grain dimensions obtained from SEM (Fig. 3) and TEM (Fig. 4) analysis, in which epitaxial recrystallization was found.

From the observed increasing trend of the broadening as a function of $1/d_{\{hkl\}}$ and the $\{hkl\}$ dependence of the broadening, the presence of micro-strain sources is also relevant in all samples. The particular dependence of the line broadening on $1/d_{\{hkl\}}$ shown in Fig. 7, suggests the presence of distributed defects, probably dislocations, even in the as-deposited sample [26–31]. The laser treatment causes a further broadening of the reflections only in case of the high fluence sample. Concomitantly to the peak broadening, also a peak shift, not shown here, was observed for this sample indicating the presence of strains at the macro level. Full quantitative analysis of the observed peak shifts and broadening is beyond the scope of this study.

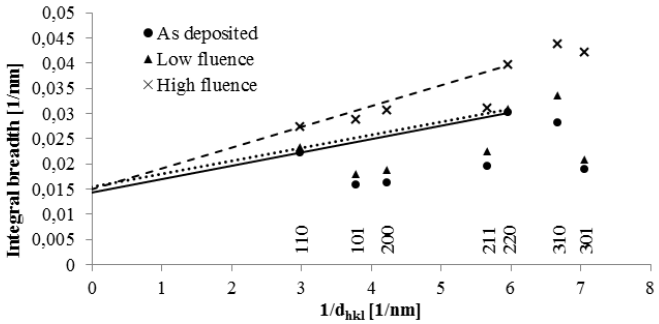

Fig. 7. Williamson Hall plot of the integral breadth versus the reciprocal lattice spacing for various SnO_2 reflections. The intercepts of the extrapolation of the line through the integral breadths of the {110} and {220} determine the size contribution to the broadening for the different samples.

#204449 - $15.00 USD Received 8 Jan 2014; revised 27 Feb 2014; accepted 28 Feb 2014; published 12 Mar 2014

3.5 Formation of defects

Positron annihilation is usually adopted to study the presence of defects, such as vacancies in materials for concentrations down to 10^{16} cm^{-3}. Signals collected by positron annihilation give information about the position of the trapping sites (lattice defects) for the positrons, thus precisely locating the extension of the affected zone where the changes observed in the SnO_2 films have a major impact on the optoelectronic properties. Laser-induced lattice defects (including Sn vacancies, ionized impurities, grain boundaries, or even substitutional atoms) lead to distortion of the lattice and act as traps or scattering centers for free carriers. In turn, these have a detrimental effect on the overall electrical properties, because these defects can induce a reduction of both the carrier density, as well as a reduced electron mobility [30]. In our samples, the measured signal will be a sum of the signals from all different contributions, from intrinsic vacancies to laser-induced defects, which play a primary role on the electrical properties.

In Fig. 8, the Doppler *S* and *W* parameters as function of the depth into the films are shown for the three samples. The S parameter gives a measure for the annihilation of positrons with valence electrons. That is, it provides information on the electronic structure of the inspected lattice and the presence of vacancies that are trapping sites for positrons. An increase of the S parameter is usually related to an increased density of defects in the lattice. The W parameter is a measure for positron annihilation with core electrons, which gives chemical sensitivity of the positron trapping site. More details on the interpretation of these parameters can be found in [14]. After measurement, the dependence of the parameters *S* and *W*, as function of depth, were analyzed using VEPFIT, which solves the implantation-diffusion equation for positrons implanted at selected energies, assuming a layered model of the sample, and fits calculated *S* and *W* curves to the experimental depth-profiles [14, 15]. From the implantation energy E [keV] and the mass density of the material ρ [g/cm^3], the average implantation depth $\langle z \rangle$ [nm] can be calculated by the equality $\langle z \rangle = 36\, E^{1.62} / \rho$.

The depth-profiles and VEPFIT analysis clearly showed that the properties of the top 130 nm layer of the as-deposited SnO_2:F film differ from the properties of the remainder of the film. That is, the thin sub-surface top 130 nm layer shows a low value of the *S* parameter of 0.4792 ± 0.0003 and high a high value of the *W* parameter of 0.0700 ± 0.0003. The layer below, towards the glass substrate, shows a relatively higher value of *S* of 0.4915 ± 0.0003 and a lower value of *W* of 0.0643 ± 0.0003, when compared to the top 130 nm layer. We attribute this difference in the top and bottom layer of the as-deposited SnO_2:F film to the large carbon fractions present in the film in the depth-range up to about 150 nm below the surface (Fig. 6), with the highest concentrations at the surface of up to 44 at% as measured by TOF-SIMS. The concentration of carbon reduces beyond a depth of about 150 nm.

Figure 8 and the VEPFIT analysis show that the treatments by low and high laser fluence lead to an increase of the *S* parameter and a reduction of the *W* parameter in the 130 to 140 nm top layer, while the *S* and *W* parameter of the layer below have smaller shifts after the laser treatments. The variations of the *W* parameter show a strong correlation with the changes in *S* parameter, and thus indicate a common origin of the cause of the changes in S and W parameter. We attribute the increase in *S* parameter, as a results of the laser treatment, to two effects. Namely, first an increase in the number of oxygen vacancies present in Sn-O vacancy complexes, which can trap positrons. And secondly, to the escape of carbon from the sub-surface region, due to laser annealing, as can be observed in Fig. 6. It is interesting to notice that the increase in the *S* parameter correlates with an increase in resistivity of the layer. The correlation resembles the trends reported by Mao *et al*. [32] for Sb-doped SnO_2 layers, where both the *S* parameter and the resistivity reduced significantly upon annealing under atmospheric conditions, leading to a reduction in oxygen vacancy concentration. In contrast, undoped SnO_2 showed an increase in resistivity due to annealing, as a result of a reduction in charge carrier concentration. Also, in the present case of doped SnO_2:F films, the changes in the charge carrier mobility, due to scattering by vacancy complexes and extended defects in the lattice, help to understand the higher resistivity of the SnO_2:F layer due to laser

#204449 - $15.00 USD Received 8 Jan 2014; revised 27 Feb 2014; accepted 28 Feb 2014; published 12 Mar 2014

annealing [30]. An explanation for the observed trend of the *S* parameter, as function of the depth in the sample treated at high laser fluence, is that the laser pulse induces a relatively high concentration of defects in top part of the film, where the resolidification from the molten state takes place. The latter is attributed to an increase of the local strain of the lattice, induced by fast quenching after irradiation. Contemporarily, also the bottom part of the layer is indirectly affected by laser processing, being attached to the highly strained top part of the layer. This is in agreement with the results of Liu et al. [33].

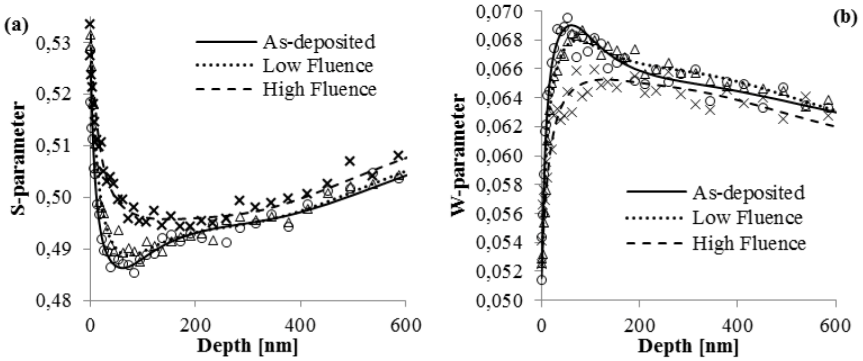

Fig. 8. a) Doppler *S*-parameter and b) *W*-parameter as a function of the average positron implantation depth profiles for as-deposited (circles), low fluence laser treated (triangles) and high-fluence laser treated (crosses) SnO_2:F films. Lines represent the fits obtained using VEPFIT.

3.6 Effects on the optical properties

The optical transmittance of the three samples was measured in the wavelength range of 400 to 1100 nm, see Fig. 9. The transmittance varies from an average value of 71.4% in the as-deposited sample to 76.1% in the sample treated at high fluence, see also Table 1. Three main causes can affect the optical transmittance of the films, namely: carbon impurities, stoichiometry and doping concentration.

Carbon impurities, either near the surface or in a TCO film, increase light absorption of the TCO over the complete range of wavelength a solar cell operates (~300-1100 nm), resulting in a lower overall efficiency of the device. In TCO's, this high absorptivity should be avoided and optical transmittance should be as high as possible. In contrast, a high concentration of carbon at the surface of the film increases the refractive index mismatch at the air-TCO interface, resulting in a higher reflectivity. Taking an average value for the optical absorption coefficient of the carbon-rich outermost layer of about 10^4 to 10^5 cm^{-1} [34] in the visible range and considering its distribution with depth, a decrease in absorption of a few percent is predicted in the sample treated at high laser fluence, which is in the same order of the experimentally observed variations in Fig. 9.

The observed decrease in the O/Sn ratio after laser annealing see Fig. 5 might also affect the optical transmittance, since the density of oxygen interstitial states (with O/Sn > 2), which absorb visible radiation, is reduced by the laser annealing.

Optical transmittance is also related to the concentration of F. In section 3.3 it was found that the initial concentration of F in the as-deposited sample was less than 0.1% at. and it varies by about 5% from the as-deposited to the sample treated at high fluence. Hence this contribution is expected to affect the total increase of transmittance to a very small extent only if compared to the observations reported in literature [35].

In conclusion, the main effect of the laser treatment on the optical properties of the SnO_2 is due to a desorption of carbon impurities from the surface. Possibly, also the changed stoichiometry can have a non-negligible effect. The desorption of carbon due to the laser processing decreases both the extinction coefficient *k* and the refractive index *n*. This is

#204449 - $15.00 USD Received 8 Jan 2014; revised 27 Feb 2014; accepted 28 Feb 2014; published 12 Mar 2014

consistent with the observed beneficial effect of the laser treatment on the increased transmittance and lowered reflectance, as measured in our previous work [1].

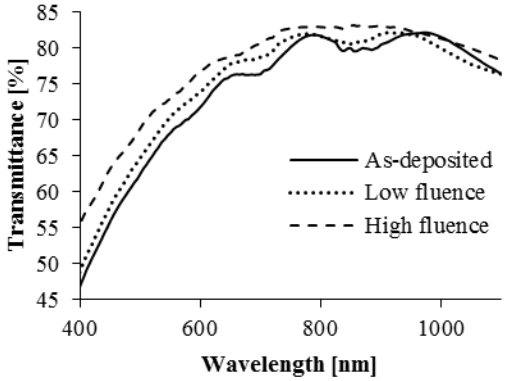

Fig. 9. Measured optical transmittance for the three samples, reproduced from [1].

3.7 Effects on the electrical properties

Hall measurements (see Table 1) show only small differences in the carrier density in the three samples, displaying a maximum value for the as-deposited sample and slightly lower values for the laser-treated samples. The Hall measurements suggest that the decrease of carrier density does not simply follow the increase of the laser fluence. That is, the carrier density of the sample treated at low fluence is lower than the value of the sample treated at high fluence. The latter observation indicates that most likely different causes do affect the carrier density with opposite effects. The total of combined effects depends on the adopted fluence regime during the laser treatment. Since the differences in the measurements are small between the three samples, we can only point out which of the measured properties can possibly play a role in the measured quantities, but not quantify the relative influence.

It is well-known that the carrier density of SnO_2 depends on point defects in the lattice associated with oxygen vacancies, which do provide free electrons in the conduction band [2]. The latter could arise from the presence of electrically active impurities acting as donors when they occupy substitutional oxygen sites, as well as from small shifts from the perfect stoichiometry, possibly caused by oxygen desorption [2]. The TOF-SIMS analysis in section 3.3, pointed out a variation in the amount of total ionized impurities, i.e. F and H, while XPS showed shifts in the stoichiometry after the laser treatment. The stoichiometric shift is relatively large, since most of the desorbed atoms are oxygen atoms which are present in excess as interstitials in the lattice above the perfect stoichiometric ratio (O/Sn = 2). Creation of intrinsic shallow donor defects can result in an increase of carrier density up to about 10^{20} cm^{-3}. Since a fraction of the observed desorbed oxygen can also originate from the lattice, hence increasing the density of oxygen vacancies, this effect is expected to increase the carrier density. Being the observed changes of the carrier density between the three samples in the order of 10^{19} cm^{-3}, stoichiometric shifts can be considered as one of the possible causes.

Resuming, on the one hand, the carrier density tends to decrease due to a slight desorption of F, but on the other hand, the laser process increases the carrier density by two factors: first, by reducing the stoichiometric ratio of O to Sn due to desorption of oxygen, and secondly, by increasing the amount of adsorbed H (see section 3.3). Presence of laser-induced defects in the lattice can also negatively affect the carrier concentration as well as the electron mobility, and will be discussed at the end of this section.

Table 1 shows a change in electron mobility, due to the laser treatment, measured by the Hall technique. A modified electron mobility in a semiconductor can arise from several causes, such as: scattering by phonons, neutral and ionized impurities, lattice defects and

#204449 - $15.00 USD Received 8 Jan 2014; revised 27 Feb 2014; accepted 28 Feb 2014; published 12 Mar 2014

grain boundaries. The total scattering rate is then the sum of the individual rates [36]. All the mentioned phenomena can be triggered by laser irradiation when a material is quickly heated and subsequently fast cooled by self-quenching. However, for a degenerate semiconductor the situation simplifies, as scattering by phonons and neutral impurities can be neglected.

The contribution of grain-boundary scattering is significant only if the grain size D_g is comparable to the mean electronic free path l_e, as determined by all scattering mechanisms [37]. In typical polycrystalline thin TCO films the mean electronic free path estimated in literature, based on the mobility and carrier concentration, is rather small-i.e. $l_e \approx 10$ nm, while $D_g \approx 100$ nm [38]. From the obtained XRD data, an estimation can be made about the effect of the laser treatment on the electron mobility of the material. Since the measured mean grain size of 67 nm as derived by XRD analysis is about one order of magnitude larger than l_e, in all the samples, we conclude that changes in electron mobility of the laser-treated samples are not due to a variation of grain boundary scattering.

In the sample treated at low fluence, where no LIPSSs were found, the main measurable effect on the electrical mobility is due to the reduction of the total amount of ionized impurities, as discussed in section 3.3. As already mentioned earlier in this section (3.7), the decreased concentration of ionized impurities affects the electronic mobility of a degenerate semiconductor. Table 1 shows the variation of the carrier densities in the three samples, which is strongly related to the density of ionized impurities in the SnO_2 matrix, such as F and H. This decreases the scattering rate from ionized impurities in the lattice and hence, increases the electron mobility. The latter can explain the slight increase of electron mobility in the low fluence sample, when compared to the electron mobility in the as-deposited sample.

Following the same reasoning, higher value of electron mobility in the sample treated at high fluence should be also expected if compared to the as deposited sample. However, Hall measurements show an opposite trend (see Table 1). Interestingly, the reduction of electron mobility is concomitant with a measured increase of strain, which was concluded from XRD data analysis. The explanation for the increased strain can be found in the formation mechanism of LIPSSs. The latter take place at high temperatures with high gradients and, when cooled down, the structured uppermost part remains strained by freezing defects in the lattice. Recent studies of SnO_2 related the effect of strain in the lattice to reduced electrical conductivity [33]. According to this report, strain in the lattice of ceramic and semiconducting materials causes elastic lattice deformation and lattice defects, such as dislocations, stacking faults and twin boundaries. The latter can trap electrons inducing electrostatic potential barriers near the trapping sites, thus reducing the carrier density and also reducing the electron mobility [31, 39].

4. Conclusions

Areas of 3 cm^2 SnO_2 films, with a thickness of 980nm, on Borofloat®-glass were irradiated by 6.7 ps, λ = 343nm laser pulses by two sets of laser conditions, referred to as low and high fluence conditions respectively: (*i*) peak fluence $F_0 = 0.17$ J/cm^2, 1 overscan, 98.7% pulse-to-pulse overlap, track-to-track pitch of 3 μm, pulse frequency of $f_p = 100$ kHz, and (ii) $F_0 = 0.26$ J/cm^2, 1 OS, OL = 98.7%, pitch = 3 μm, $f_p = 100$ kHz. We observed two main different regimes as results of the laser treatment for the two laser treated samples. While at low fluence the SnO_2 layer remained completely in solid state, showing no changes in the surface morphology, the sample treated at high fluence showed that the top layer of 100-200 nm of the SnO_2 film was subjected to melting and resolidification. The latter was concluded on the basis of observed Laser-induced Periodic Surface Structures (LIPSSs). Careful analysis revealed a total absence of amorphous material, even in the outermost atomic layers of both laser treated samples. A tuning of the laser parameters (such as F_0, f_p and OL) was necessary to achieve the optimal inter-pulse heat accumulation, which slows down the resolidification process and avoids amorphization. Simultaneously, the heat accumulation was moderate, which ensured a thermally damage-free film and substrate. The latter is an essential condition

#204449 - $15.00 USD Received 8 Jan 2014; revised 27 Feb 2014; accepted 28 Feb 2014; published 12 Mar 2014

to exploit ultra-short pulsed lasers for ultra-shallow thermal treatments even above the melting threshold of the material without damaging the structure of the lattice.

Our investigation revealed multiple effects of the laser treatment on the properties of the SnO_2 film, where small changes in the observed macroscopical optoelectronic properties can arise from several combined different phenomena, whose contributions cannot be isolated easily. Chemically, desorption of fluorine was measured as well as of oxygen, which induce shifts in the stoichiometric O/Sn ratio after the laser treatment. Carbon contaminant impurities at the top surface was also reduced after the laser treatment. On the other hand, adsorption of hydrogen from surrounding atmosphere was measured. The presence of laser-induced lattice defects, related to different strains observed in the film, was found in the case of the sample treated at high laser fluence. Those defects are likely created during the rapid self-quenching phase of the process. That is, the velocity of the solid/melt interface is sufficiently high to 'freeze' those defects in the lattice, which in turn generates strain in the film. Depending on the laser processing conditions, each of these contributions can play an important role or even dominate the final opto-electronic properties of the films.

In the two laser treated samples, different properties were identified in the top 100 to 200 nm layer of the SnO_2 films, when compared to the remaining layer of the film on glass. This difference is sharper in the sample treated at high fluence, where fast resolidification from the molten state has occurred, than in the sample treated at low fluence. This observation indicates that changes in the opto-electronic properties can be mainly attributed to the top 100 to 200 nm layer of the film and only secondarily to the rest of the layer, which remains almost unaffected by the laser annealing.

Finally, the overall performance of the SnO_2 films before and after the laser treatment were compared via the figure of merit $\phi = T^{10} / R_{sh}$. It was found that the ϕ of already industrially optimized SnO_2 films was increased up to 59% due to laser processing.

Acknowledgments

We acknowledge financial support for this research from ADEM, A green Deal in Energy Materials of the Ministry of Economic Affairs of The Netherlands (http://www.adem-innovationlab.nl).

#204449 - $15.00 USD Received 8 Jan 2014; revised 27 Feb 2014; accepted 28 Feb 2014; published 12 Mar 2014